

Geophysical Research Letters[®]



RESEARCH LETTER

10.1029/2023GL103848

Key Points:

- We have observed and reconstructed for the first time a three-dimensional undulated quasi-perpendicular bow shock surface
- The undulated shock surface resulted from a shock-discontinuity interaction
- The reconstructed saddle-shaped shock undulation predicts a jet narrow along magnetic field and stretched perpendicular to the field

Supporting Information:

Supporting Information may be found in the online version of this article.

Correspondence to:

C. Shen,
shenchao@hit.edu.cn

Citation:

Zhou, Y., Shen, C., & Ji, Y. (2023). Undulated shock surface formed after a shock-discontinuity interaction. *Geophysical Research Letters*, 50, e2023GL103848. <https://doi.org/10.1029/2023GL103848>

Received 24 MAR 2023

Accepted 24 APR 2023

Author Contributions:

Conceptualization: Yufei Zhou
Data curation: Yufei Zhou
Formal analysis: Yufei Zhou
Funding acquisition: Chao Shen
Investigation: Yufei Zhou
Methodology: Yufei Zhou
Project Administration: Chao Shen
Resources: Yufei Zhou
Software: Yufei Zhou
Supervision: Chao Shen
Validation: Yufei Zhou
Visualization: Yufei Zhou
Writing – original draft: Yufei Zhou
Writing – review & editing: Yufei Zhou, Chao Shen, Yong Ji

© 2023. The Authors.

This is an open access article under the terms of the [Creative Commons Attribution License](https://creativecommons.org/licenses/by/4.0/), which permits use, distribution and reproduction in any medium, provided the original work is properly cited.

Undulated Shock Surface Formed After a Shock–Discontinuity Interaction

Yufei Zhou¹ , Chao Shen¹ , and Yong Ji¹ 

¹Harbin Institute of Technology (Shenzhen), Shenzhen, China

Abstract Shock ripples and shock–discontinuity interactions (SDIs) have long been proposed to explain the frequent occurrence of high-speed jets (HSJs) in the magnetosheath; however, there is no direct observational evidence for either of them occurring near a shock. Herein, we report a large-scale, long-duration undulated quasi-perpendicular shock surface that is capable of generating HSJs. Based on the curvatures estimated for the shock undulation and for a nearby hot flow anomaly (HFA), we suggest that the shock ripple mechanism and the SDI mechanism combine to generate HSJs, that is, during an SDI, shock undulations and an upstream HFA form simultaneously, and the solar wind between them is deflected by the undulation into jets. The HSJs, discontinuity, and HFA are then convected downstream. An HSJ consistent with our mechanism in another event is presented.

Plain Language Summary High-speed jets are transient structures in the Earth's magnetosheath downstream of the Earth's bow shock. A high-speed jet can have a dynamic pressure greater than that of the ambient solar wind in the magnetosheath. In some cases, this dynamic pressure can even surpass that of the upstream solar wind. Thus, a high-speed jet can have a strong impact on the magnetopause, for example, by indenting it over a large spatial scale, exciting eigenmode waves, or triggering a magnetic reconnection. Furthermore, a high-speed jet can have a significant impact on the geomagnetic environment. It has been independently suggested that shock ripples can explain the origin of high-speed jets, as can shock–discontinuity interactions. However, despite the wide acceptance of these two mechanisms, there is a lack of direct observational data from near a shock to support either. Using multipoint measurements, we present for the first time evidence that, following its interaction with a solar wind discontinuity, the bow shock becomes deformed/undulated over a large scale for a long duration, which can produce a high-speed jet. Thus, we suggest that both mechanisms combine to generate high-speed jets.

1. Introduction

High-speed jets (HSJs) are transient structures that are abundant in the Earth's magnetosheath, and they have been of particular interest to the space physics community for more than a decade. A high-speed jet could have a dynamic pressure greater than that of the ambient solar wind in the magnetosheath. This dynamic pressure, though not typically, can even surpass that of the upstream solar wind. Thus, a high-speed jet can have a strong impact on the magnetopause (Archer et al., 2019; Hietala et al., 2018; Plaschke et al., 2018). They can even accelerate electrons (Liu et al., 2019).

Among other mechanisms for generating HSJs (Kajdič et al., 2021; Omelchenko et al., 2021; Raptis et al., 2022), the two most commonly recognized are shock ripples (Hietala et al., 2009) and shock–discontinuity interactions (SDIs) (Archer et al., 2012; Savin et al., 2012). The former has been suggested as being responsible for most observed HSJs. Because quasi-parallel shocks are inherently rippled in comparison with quasi-perpendicular shocks, which are usually planar beyond kinetic scales, the ripple mechanism has been suggested to occur in quasi-parallel shocks. Computer simulations suggest that a rippled quasi-parallel shock can deflect the inflow from upstream and focus it into a jet (Hao et al., 2016; Preisser et al., 2020). Moreover, kinetic ripples of 1–3 ion inertial lengths on quasi-perpendicular shocks have been identified in measurements made by the Magnetospheric Multiscale Mission (MMS) (Gingell et al., 2017; Johlander et al., 2016). However, there is still a lack of direct observational evidence that the ripples are large enough and stable long enough to produce the observed HSJs.

The SDI mechanism, however, associates an HSJ either with a rotational discontinuity transmitted downstream following its interaction with the shock or with a hot flow anomaly (HFA) produced by an SDI. This mechanism

works for both quasi-parallel and quasi-perpendicular shocks. It has been suggested that SDIs produce a relatively small number of quasi-perpendicular HSJs. According to three recent studies (Goncharov et al., 2020; Raptis et al., 2020; Vuorinen et al., 2019), the number of quasi-perpendicular HSJs may be one-ninth, one-fourth, or one-half that of quasi-parallel HSJs, respectively. Large-amplitude HSJs are often associated with discontinuities (Hietala & Plaschke, 2013). Recent single-event studies have reported that following the passage of solar wind discontinuities, powerful HSJs can cause large indentations in the magnetopause and excite sinusoidal surface waves. They may trigger reconnections (Archer et al., 2019; Escoubet et al., 2020). In the heliospheric context, because of the Parker spiral (Parker, 1958), the termination shock and the bow shock (BS) of the outer planets are more frequently quasi-perpendicular. This mechanism, therefore, deserves further study. Nonetheless, like the ripple mechanism, there is also a lack of direct observation that SDIs produce HSJs.

In this letter, using fortuitous multipoint spacecraft observations made during an SDI and a recently developed analysis method called normal field analysis (NFA) (Shen et al., 2020), we present the first observational evidence for a three-dimensional, large, stable undulation on the BS surface in support of the shock ripple mechanism. The large-scale shock undulation and an HFA appear to be byproducts of the SDI. Therefore, we suggest that the effects combined could form a downstream HSJ. In Appendix B, we present the details and an error analysis of all of the analysis methods utilized in this study.

2. Observations

We analyzed measurements made by Cluster (Escoubet et al., 2001) and Advanced Composition Explorer (ACE) (Stone et al., 1998) around midnight on 8 February 2002. The four Cluster spacecraft, C1–C4, were close to the dayside quasi-perpendicular BS, and three consecutive crossings of shock surfaces were observed. The Cluster constellation was relatively compact along the x -direction, with a scale of 45 km, but elongated in the y – z plane, with a scale of 100 km. We used data from the magnetic field measurements with FGM (Balogh et al., 1997) on all four of the spacecraft and from the CIS-HIA ion experiment on C1 (Rème et al., 1997). Information about the pristine solar wind and magnetic field was provided by the SWEPAM (McComas et al., 1998) and the MFI (Smith et al., 1998) on ACE, which was at the L1 point.

The upstream solar wind flowed steadily at $V \approx 500$ km/s with a dynamic pressure close to 1.6 nPa (Figure 1e). Embedded in the solar wind were discontinuities that recurred about every 10 min. The interplanetary magnetic field rotated abruptly across these, although its magnitude remained unchanged (Figures 1a and 1b). The near zero motion of the discontinuities relative to the background solar wind (Artemyev et al., 2019; Horbury et al., 2001) was confirmed by comparing the time-shifted magnetic field measured by ACE with that measured by C1 (Figures 1c and 1d). This suggests that they were tangential discontinuities, although we will refer to them as directional discontinuities (DDs) in this study. Two special DDs (DD-A and DD-B) were delineated by dashed vertical lines, and we will discuss them later.

The Cluster spacecraft, moving on an outbound orbit in the north-dusk side sheath, encountered an HSJ near 00:14 (Figure 1e). Later, they were passed by the BS at the geocentric solar ecliptic (GSE) $(12.2, 7.7, 7.0)R_E$ at 00:24 UT with a relative speed of 13 km/s (estimated using four-spacecraft timing, Harvey, 1998) during an Earthward motion. In the near upstream region, Cluster encountered an HFA, which was characterized by a higher temperature, a lower density, a slowing down of the flow (Figure 1f), and two fast shocks, one at the leading edge and one at the trailing edge. This HFA was mature, which can be confirmed by the cuts of 3D distribution function of ions (not shown).

The BS crossings by C1–C4 were almost simultaneous (Figure 1h), yet the recorded four local surface normals as determined by MVAB (Bengt U. Ö. Sonnerup & Maureen Scheible, 1998) (Table 1) differed from each other to a large extent, and the mean difference was $|\Delta \mathbf{n}| = 9^\circ$. This suggested that the local shock surface near these crossing points was severely curved. Based on the estimated local normals and NFA, and through the procedures described in Appendix A, we obtained the principal curvatures and directions of the undulated surface and reconstructed the surface.

The undulated surface is shown in Figure 2a. Its first principal direction, $\hat{\mathbf{x}}_1$, was almost perpendicular to the local magnetic field and along the z -direction in GSE coordinates (Table 1). Along this direction, the undulated surface had a principal curvature of $-6.7R_E^{-1}$, which indicated that it had bent downstream on a scale of $0.3R_E$ (1,900 km or 19 ion inertial lengths). The second principal direction, $\hat{\mathbf{x}}_2$, was within 10° of the local magnetic vector and

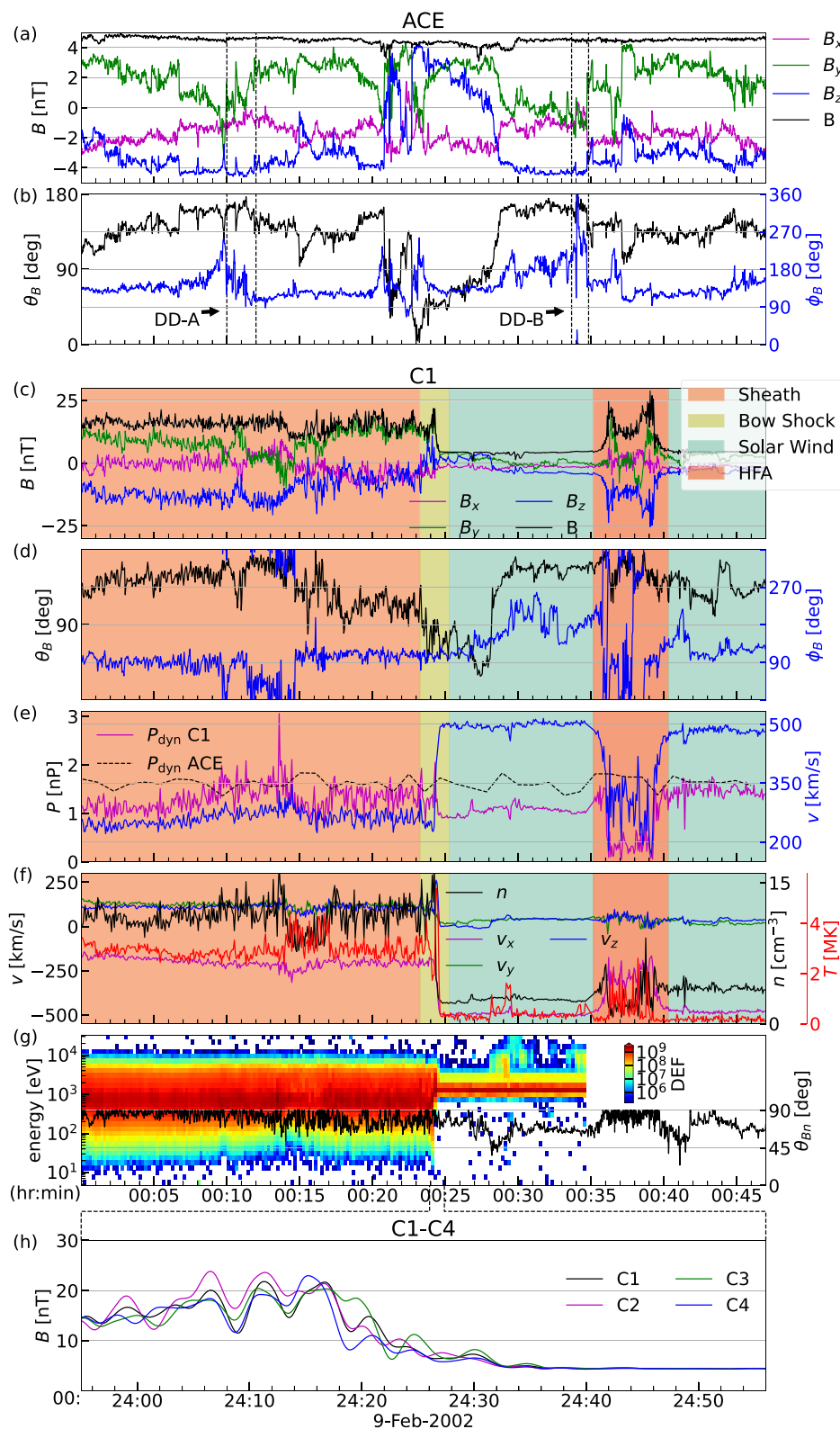


Figure 1.

Table 1
Geometric Parameters of the Shock Undulation

GSE	Local normal				Curvature and direction		
	C1	C2	C3	C4	$\kappa_1 = -6.7R_E^{-1}$	$\kappa_2 = 4.9R_E^{-1}$	\hat{x}_3
<i>x</i>	0.989	0.975	0.977	0.982	−0.059	−0.118	0.984
<i>y</i>	0.124	0.220	0.203	0.152	0.362	0.959	0.175
<i>z</i>	0.079	0.012	−0.066	−0.109	−0.930	0.257	−0.021

close to the *y*-direction. Along this direction, the surface was bent upstream. The bending, which was on a spatial scale of $0.4R_E$, was akin to that in the other direction.

Accurately estimating the geometric parameters of a local shock surface requires it to be stable during a crossing. The error analysis for NFA in Appendix B confirms the accuracy, which indicates that the undulated surface changed only slightly during the ~ 1 min of the crossing. Therefore, this non-planar shock surface is capable of modifying the flow structure consistently on a spatial scale of $0.4R_E$ perpendicular to the flow and on a temporal scale beyond 1 min. Note that this temporal duration is not the duration of HSJs identified from spacecraft observations using various criteria (Plaschke et al., 2018).

Similarly, we were able to recover the HFA surface. Using magnetic field data for the leading (Earthward) and trailing (Sunward) edges of the HFA, we obtained their respective geometric parameters. Figure 2b shows, in the local coordinate system, a sketch of the imaginary extension of the undulated shock surface, the HFA, and the trajectory of Cluster. The global normals of the leading and trailing edges of the HFA were (0.974, 0.066, 0.215) and (0.968, 0.221, 0.116), respectively. Both of them were nearly parallel to the BS normal. The principal curvatures of the leading edge were $1.1R_E^{-1}$ and $2.8R_E^{-1}$, whereas those of the trailing edge were $-6.3R_E^{-1}$ and $-4.3R_E^{-1}$. This indicated that both of the edges were spherelike and bent toward the core of the HFA. The leading edge was larger ($1R_E$) than the trailing edge ($0.4R_E$). The principal directions were degenerate, possibly because the edges were expanding due to being driven by the thermal pressure in the core. Thus, they were not stationary enough during the spacecraft crossing.

3. Interpretation and Discussion

Note that the HFA had a trailing-edge (radius of) curvature close to that of the shock undulation. This implied that the ways in which they were respectively formed were closely related. In fact, the geometric parameters obtained from the event were consistent with those from the canonical theory for the formation of an HFA by SDI (Burgess & Schwartz, 1988; S. Schwartz, 1995; Zhao et al., 2015). This theory has, so far, not accounted for the role of shock undulations. Here, according to our findings, we present a new overall scheme for shock undulations and HFA formation during such an interaction and for the subsequent formation of an HSJ.

An HFA usually occurs when a discontinuity is at a large oblique angle to the BS and the electric field points toward it on at least one side (Burgess & Schwartz, 1988; S. Schwartz, 1995; Zhao et al., 2015). The results for the MVAB performed on the various discontinuities visible in Figures 1a and 1b and the electric field calculated through $-\mathbf{V} \times \mathbf{B}$ indicated that only DD-A and DD-B satisfied these criteria. The normal of DD-A differed by 75.8° from the global normal of the BS crossed by Cluster. That difference for DD-B was 74.2° . Additional comparison between the direction of the magnetic field vector observed by ACE across DD-B (Figure 1b) and those observed by C1 across the HFA (Figure 1d) suggested that DD-B was embedded in the HFA. Therefore, DD-B caused the undulated BS surface and the upstream HFA.

Figures 2b and 2c illustrate the overall mechanism. Consider a directional discontinuity moving toward a shock and assume that their normals differ by a large angle. At their intersection, the ions specularly reflected from the

Figure 1. Advanced Composition Explorer (ACE) magnetic field data in (a) geocentric solar ecliptic (GSE) Cartesian coordinates and (b) GSE spherical coordinates (time-shifted by 41 min to account for solar wind propagation to the bow shock (BS)). Two special directional discontinuities are delineated by dashed vertical lines and annotated as DD-A and DD-B. In (c)–(f), color shadings mark different plasma regions. C1 magnetic field data in (c) GSE Cartesian coordinates and (d) GSE spherical coordinates. (e) Solar wind dynamic pressure and speed from C1 and dynamic pressure from ACE. (f) Ion velocity, number density, and temperature from C1. (g) Ion omnidirectional differential energy fluxes ($\text{keV cm}^{-2} \text{s}^{-1} \text{sr}^{-1} \text{keV}^{-1}$) over-plotted with the angle between the local magnetic field and the BS normal. (h) Magnetic field magnitude from C1–C4 during the BS crossing.

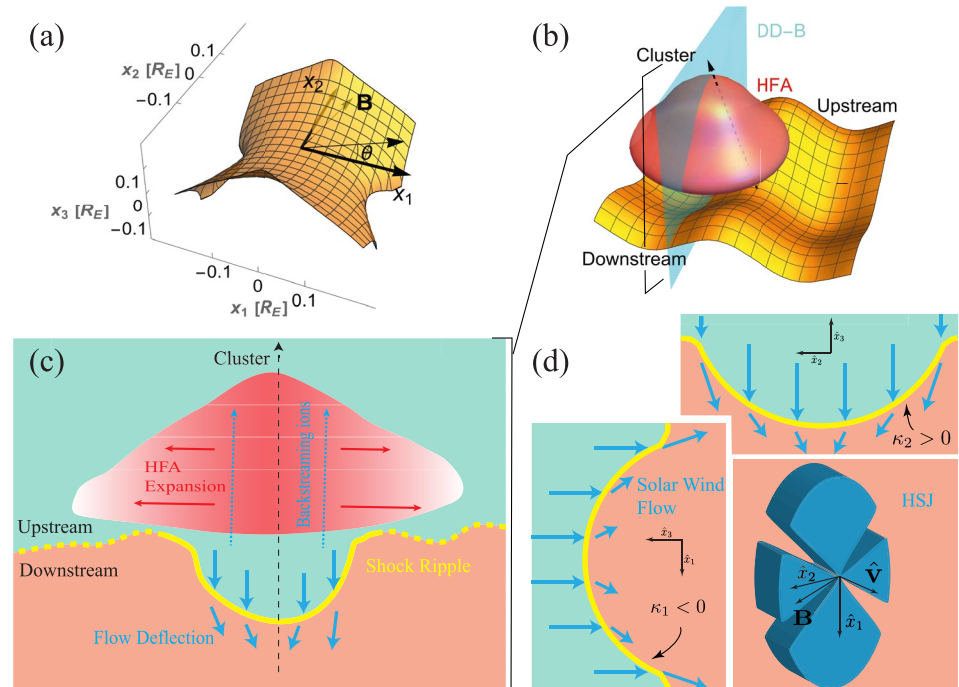


Figure 2. (a) Reconstructed BS undulation in the intrinsic coordinate system of the local surface. (b) Imaginary extension of the undulated surface, the (red) hot flow anomaly (HFA) and (cyan) discontinuity DD-B encountered by Cluster (dashed arrow). (c) Illustration of the formation of a shock undulation and HFA during shock–discontinuity interaction (SDI). The high-speed jet (HSJ) was generated due to the shock curvature. (d) Illustration of the effect of the undulated shock geometry on the HSJ morphology and the predicted cross section of the HSJ downstream of the observed shock undulation.

shock were channeled along the discontinuity deep into the pristine solar wind, where they triggered instabilities, resulting in the creation of a heated region, that is, an HFA (Burgess, 1989; Zhang et al., 2010). The initial spatial extent of the region perpendicular to the path of the reflected ions should be consistent with that of the ions, which we inferred was $0.4R_E$ during the event. During the journey of the backstreaming ions, the region near the shock was heated first, while the more distant regions followed. Because the pressure of the previously heated region was well beyond ambient, it expanded to a greater extent (giving the leading edge of $1R_E$) than the subsequently heated region was able to, given the limited time available.

At the same time, the local shock surface near the intersection between the bow shock and the discontinuity deformed due to the loss of reflected ions that would otherwise gyrate back to the shock (Thomas et al., 1991). The deformation of the BS was on the same scale as the reflected ion population, which is why the shock undulation also had a scale of $0.4R_E$. After this deformation, the flow between the HFA and the shock undulation was deflected during its transmission across the shock due to the curvature of the shock surface. Note that as shown in Figures 1e and 1f, the flow between the BS and HFA had a higher temperature and lower density than that upstream of the trailing edge of the HFA. This suggested that the flow had already been affected by the SDI. As the HFA became convected by the solar wind toward the downstream region, the deformation of the shock surface was even steeper, so that it was less effective in braking the solar wind near the HFA. An HSJ could therefore form and propagate accompanying the discontinuity and the HFA. During propagation, the coherent structure of the HFA and the discontinuity, however, could dissolve, leaving only scattered bumps and dips in the ion density, temperature, and electric current density (Eastwood et al., 2008).

Direct confirmation of the predicted formation of the HSJ during this event would require an additional spacecraft downstream, which was unfortunately not available. Here, we point out an HSJ that was consistent with our mechanism in a separate event identifiable from the magnetosheath observation shown in Figure 1. Near 00:15, C1 observed features in the ion density and temperature that were almost the same as those of the upstream HFA. This was an HFA that was yet to diffuse in the magnetosheath. Preceding it was the discontinuity DD-A (observed by ACE), which could have interacted with the BS in the same way as discussed above. The speed

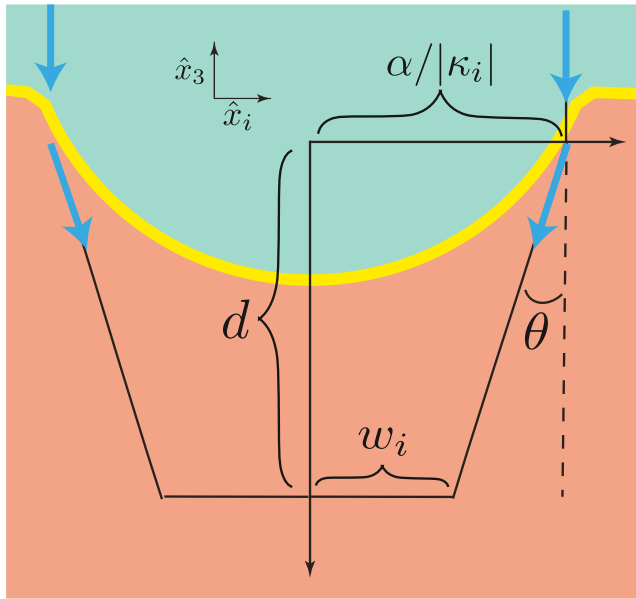


Figure 3. Prediction of the size of the HSJ near the shock from the curvature of the shock undulation.

of the shocked flow increased toward the magnetosheath HFA and peaked around it (Figure 1e). The density, due to an accumulation of the flow on the leading edge of the HFA and flow concentration caused by deflection of the shock undulation, peaked just before the HFA. The coinciding of the density and velocity peaks resulted in the HSJ.

Now that we have reconstructed the undulated shock surface, another problem of interest is which properties of the HSJ can be predicted with it. Through a simple calculation, we show that in regions not far from the shock, the cross-sectional area and density of the HSJ were determined by the mean and Gaussian curvature of the undulation and that the properties of the HSJ predicted from the observed undulation were in agreement with statistical studies of the HSJ morphology.

As illustrated in Figures 2d and 3, we assume that the solar wind is from \hat{x}_3 , which is a good approximation for the event. We also assume that the local shock surface reconstruction is valid when $|x_i| < \alpha/|\kappa_i|$, $i = 1, 2$, where α is a controlling parameter. Because the surface has two principal directions, the cross section of the HSJ has two independent half-widths w_i , which are, in effect, the distances from the HSJ boundary flows to the x_3 -axis. As shown by the geometry in Figure 3, they are related to the propagation distance d of the HSJ as follows:

$$w_i = \text{sgn}(\kappa_i) d \tan \theta + \alpha/|\kappa_i|, \quad i \in \{1, 2\}, \quad (1)$$

where

$$\tan \theta = \left| \left(1 - \frac{2}{r} \right)^{1/2} \hat{\mathbf{v}}_u \cdot \frac{\nabla F}{|\nabla F|} \right|_{x_1=\alpha/\kappa_1, x_2=0},$$

θ is the deflection angle of the boundary flow, r is the shock compression ratio, $\hat{\mathbf{v}}_u$ is the upstream velocity direction, and F is the function for shock surface defined in Appendix A. This expression for the half-width of the HSJ is valid until the jet is compressed to the extent that the boundary flow cannot squeeze it any further. Let the cross-sectional area $S = \pi w_1 w_2$. Based on mass conservation, $S(d)\rho(d) = S_0\rho_0$, where 0 denotes the value at the shock, we can obtain the density determined by the mean curvature of the local shock surface $H = (\kappa_1 + \kappa_2)/2$ and the Gaussian curvature $K = \kappa_1\kappa_2$ as

$$\rho(d) = \frac{\rho_0}{(1 - 2Hsd + Ks^2d^2)}, \quad (2)$$

where $s = (1/\alpha)\tan\theta$.

During the event, the two curvatures had similar magnitudes and opposite signs, which together indicated that the cross-sectional shape of the HSJ was circular near the BS and elliptical further downstream (Figure 2d). We assume that $\alpha = 0.99$, so that the angle between the upstream velocity and the shock normal at the undulation boundary was 98° . After propagating $1R_E$, the scales of the HSJ along and perpendicular to the magnetic field were $0.2R_E$ and $0.5R_E$, respectively. Its density was 1.7 times the background (note that the ultimate shape of the HSJ was not sensitive to the choice of α). This was consistent with and possibly explained the origin of the HSJs reported by Gutynska et al. (2015), which, on average, had a density enhancement ratio greater than 1.5, a magnetic-parallel scale of $0.3R_E$, and a magnetic-perpendicular scale of $0.8R_E$. The size predicted here was also consistent with other statistical studies that assumed that the cross section was circular a priori and predicted a most probable diameter of $0.1R_E$ and $0.5R_E$ (Archer et al., 2012; Plaschke et al., 2020). In addition to the elliptical section, the negative Gaussian curvature also indicated that along intermediate directions on the undulated surface, the curvatures were near zero such that an HSJ could not be produced there. The resulting section of the overall HSJ resembled a set of rotor blades.

In previous simulations of the interactions between a shock and discontinuities (Omidi & Sibeck, 2007; Omidi et al., 2020), as shown in their figures, the jets were indeed downstream of the shock undulations. However, no

attention was paid to their relations. Moreover, extensive studies have focused on quasi-parallel shocks, which are highly rippled because of their interactions with foreshock structures, as seen in simulations (see, e.g., Hao et al., 2016; Guo et al., 2022). Limited attention has been paid to the possibility that, for quasi-perpendicular shocks, the ripple mechanism could explain the cause and effect of the SDI mechanism. The scheme presented here is a combination of the two and, in effect, an overall description of an SDI.

One interesting feature in the event is that one principal direction of the shock undulation was almost aligned along the magnetic field. This hinted at an important role that the field may play in the formation of the undulation. However, to ascertain this would require additional statistical studies and three-dimensional (3D) simulations.

For a Sun-like rotating magnetized star that emits a supersonic stream, the interplanetary magnetic field lines are twisted and in the shape of an Archimedean spiral (also known as a Parker spiral). Further away from the star, the magnetic field becomes increasingly perpendicular to the stream and parallel to the shocks that are formed following the interaction of the stream with obstacles, such as a planetary magnetic field or an interstellar medium. In the heliosphere, the termination shocks and the subsolar BSs of planets beyond Mars are all of this nature. The mechanism put forward herein can be applied to these quasi-perpendicular shocks.

Although SDIs were previously observed and simulated for quasi-perpendicular shocks (Thomas et al., 1991; S. J. Schwartz et al., 2000; Lin, 2002), more recent observations and simulations have suggested that they are more likely to occur with quasi-parallel shocks (Facsó et al., 2009; Omid & Sibeck, 2007; Wang et al., 2013). Our mechanism, thus, can also be used for HSJs in a quasi-parallel magnetosheath. Depending on factors such as the solar wind speed, discontinuity thickness, electric fields on both sides of the discontinuity, inclination angle of the discontinuity to the BS, and rotation angle of the magnetic field across the discontinuity, the efficiency of the interaction varies and its spatial size could be $0.2R_E$ – $5R_E$ (see, e.g., S. J. Schwartz et al., 2000; Facsó et al., 2009; Zhao et al., 2017). Shock undulations and HSJs of this size are hence expected.

4. Conclusions

In summary, we have observed and reconstructed for the first time the three-dimensional surface of an undulated shock front that is large enough to produce HSJs in the magnetosheath. On this basis, and with curvatures estimated for an upstream HFA, we have postulated an overall scenario for the generation of HSJs after an SDI. An undulated shock surface and an HFA are formed simultaneously during the interaction. After that, the undulated shock deflects the pristine solar wind between it and the HFA but without much braking and focuses them into a jet. Then, the HSJ, discontinuity, and HFA convect downstream. The cross section of the HFA predicted from the observed shock undulation is narrow along the magnetic field lines and elongated perpendicular to the field lines.

Appendix A: Reconstructing a Local Surface

The local geometry of a surface is determined by its two principal directions and the corresponding principal curvatures (Kühnel & Hunt, 2015). From the principal directions, which are perpendicular to one another, a local coordinate system can be constructed, as shown in Figure 2a. The x_3 -axis is defined by the global surface normal. The x_1 -axis is defined by the principal direction along which the curvature is at a minimum, and the x_2 -axis by the principal direction along which the curvature is at a maximum. Principal curvatures can be either positive, corresponding to a surface bending along the corresponding direction toward the surface normal, or negative, corresponding to a surface bending away from the surface normal. The bending (or curvature) along an intermediate direction on the surface, characterized by the polar angle $\theta = \arctan(x_2/x_1)$, is obtained through Euler's formula:

$$\kappa = \kappa_1 \cos^2 \theta + \kappa_2 \sin^2 \theta, \quad (\text{A1})$$

where κ_1 and κ_2 denote the minimum and maximum curvatures, respectively. Since curvatures along all of the directions on the surface can be found from this equation, by defining

$$F(x_1, x_2, x_3) = x_1^2 + x_2^2 + \left(\frac{1}{\kappa} - x_3\right)^2 - \frac{1}{\kappa^2}, \quad (\text{A2})$$

the local surface can be reconstructed from $F(x_1, x_2, x_3) = 0$. The principal directions and curvatures of a local shock surface from multi-spacecraft observations can be found with NFA under the assumption that the shock

surface is stable on the timescale of a spacecraft crossing (see Supporting Information S1 for a brief description of the method).

Appendix B: Error Analysis

Here, we present the details and the error analysis of the MVAB as well as the timing and NFA calculation.

B1. Bow Shock

For every BS crossing by a spacecraft, we performed MVAB to estimate the local normal of the shock at the crossing point. We chose the interval for analysis by centering it at the steepest point of the magnetic field magnitude and extending it by 1 min in each direction to cover a sufficient range of the downstream and upstream regions. The center points for C1–C4 were at 24:15.5 (min:sec), 24:15.1, 24:19.7, and 24:15.1, respectively. The results are shown in Table 1. The number of points on average was 2,147, and the ratio r_λ averages 2.3. Using the analytical estimation method (for detail, see Chap. 8.3.1 of Bengt U. O. Sonnerup & Maureen Scheible, 1998), the statistical error for the estimated normals is

$$|\delta \mathbf{n}| = \sqrt{r_\lambda / (M - 1)} / (r_\lambda - 1) = 1.5^\circ,$$

which was considerably less than the difference $|\Delta \mathbf{n}| = 9^\circ$ for the estimated normals. The above-mentioned center points were used in the timing analysis to provide a shock speed relative to the spacecraft of 13 km/s.

The systematic error originating from the temporal evolution of the undulation on the shock surface is difficult to estimate. However, we can assess the error based on the results from NFA. If the undulation is transient on the timescale of a spacecraft traversal, the surfaces crossed at different times are not the same, making it difficult to determine the principal curvatures and directions. The inconsistencies in these normals would compromise the orthogonality between the three eigenvectors estimated by NFA, which was not the case for the event shown in Table 1. The average deviation from 90° of the angles among $\hat{\mathbf{x}}_1$, $\hat{\mathbf{x}}_2$, and $\hat{\mathbf{x}}_3$ was $|e_{\text{NFA}}| = 3.6^\circ$, which indicates high accuracy.

B2. Hot Flow Anomaly (HFA)

The same analysis was applied to the leading and trailing edges of HFA-B. We chose for the former 36:9.6, 36:9.2, 36:3.3, and 36:9.0 and for the latter 39:19.0, 39:18.4, 39:25.9, and 39:18.6 as the center points for the MVAB. The statistical errors of both were $|\delta \mathbf{n}| = 1.1^\circ$. The difference for the estimated normals of the trailing edge was $|\Delta \mathbf{n}| = 13.0^\circ$, which satisfied $|\Delta \mathbf{n}| \gg |\delta \mathbf{n}|$. For the leading edge, the difference was $|\Delta \mathbf{n}| = 3.9^\circ$, which, though not much larger than the error, did not impair the conclusion that this surface was less curved than the other two. The error indicator $|e_{\text{NFA}}|$ in the NFA was larger at 30.9° and 35.3° than that for the BS undulation, probably because the two edges were expanding and because there was a systematic inconsistency in the four estimated normals.

B3. Directional Discontinuity B

To determine the normal of DD-B, MVAB was applied to the data measured by ACE delineated by the dashed lines in Figure 1 from 33:40 (min:sec) to 34:50 (note that the data was time-shifted by 41 min). The result was [0.306, −0.047, 0.951]. The ratio $r_\lambda = \lambda_2/\lambda_3$ was 15.1. $M = 70$ points were used. The statistical error for the estimated normals was 1.9° .

B4. Directional Discontinuity A

MVAB was applied to the ACE data delineated by the dashed lines in Figure 1 from 10:00 (min:sec) to 12:00. This shows that the normal of DD-A was [0.316, −0.274, 0.908]. The ratio r_λ was 7.2. The statistical error for the estimated normal was 2.3° .

Data Availability Statement

The magnetic field data set from the Cluster mission is available at <https://csa.esac.esa.int/csa-web/#search> and can be found by searching FGM in CLUSTER MISSION EXPERIMENTS. The ACE magnetic field data set is available at https://cdaweb.gsfc.nasa.gov/pub/data/ace/mag/level_2_cdaweb/mfi_h3/ and the particle data set is available at https://cdaweb.gsfc.nasa.gov/pub/data/ace/swepam/level_2_cdaweb/swe_h0/.

Acknowledgments

This work was supported by the National Natural Science Foundation of China under Grants 42130202 and 41874190 and the National Key Research and Development Program of China under Grant 2022YFA1604600. We thank CDAWeb and the Cluster Active Archive for data access.

References

- Archer, M. O., Hietala, H., Hartinger, M. D., Plaschke, F., & Angelopoulos, V. (2019). Direct observations of a surface eigenmode of the dayside magnetopause. *Nature Communications*, 10(1), 615. <https://doi.org/10.1038/s41467-018-08134-5>
- Archer, M. O., Horbury, T. S., & Eastwood, J. P. (2012). Magnetosheath pressure pulses: Generation downstream of the bow shock from solar wind discontinuities. *Journal of Geophysical Research*, 117(A5), A05228. <https://doi.org/10.1029/2011JA017468>
- Artemyev, A. V., Angelopoulos, V., Vasko, I. Y., Runov, A., Avakov, L. A., Giles, B. L., et al. (2019). On the kinetic nature of solar wind discontinuities. *Geophysical Research Letters*, 46(3), 1185–1194. <https://doi.org/10.1029/2018GL079906>
- Balogh, A., Dunlop, M. W., Cowley, S. W. H., Southwood, D. J., Thomsen, J. G., Glassmeier, K. H., et al. (1997). The cluster magnetic field investigation. *Space Science Reviews*, 79(1/2), 65–91. <https://doi.org/10.1023/A:1004970907748>
- Burgess, D. (1989). On the effect of a tangential discontinuity on ions specularly reflected at an oblique shock. *Journal of Geophysical Research*, 94(A1), 472. <https://doi.org/10.1029/JA094iA01p00472>
- Burgess, D., & Schwartz, S. J. (1988). Colliding plasma structures: Current sheet and perpendicular shock. *Journal of Geophysical Research*, 93(A10), 11327. <https://doi.org/10.1029/JA093iA10p11327>
- Eastwood, J. P., Sibeck, D. G., Angelopoulos, V., Phan, T. D., Bale, S. D., McFadden, J. P., et al. (2008). THEMIS observations of a hot flow anomaly: Solar wind, magnetosheath, and ground-based measurements. *Geophysical Research Letters*, 35(17), L17S03. <https://doi.org/10.1029/2008GL033475>
- Escoubet, C. P., Fehringer, M., & Goldstein, M. (2001). Introduction: The cluster mission. *Annales Geophysicae*, 19(10/12), 1197–1200. <https://doi.org/10.5194/angeo-19-1197-2001>
- Escoubet, C. P., Hwang, K.-J., Toledo-Redondo, S., Turc, L., Haaland, S. E., Aunai, N., et al. (2020). Cluster and MMS simultaneous observations of magnetosheath high speed jets and their impact on the magnetopause. *Frontiers in Astronomy and Space Sciences*, 6, 78. <https://doi.org/10.3389/fspas.2019.00078>
- Fascio, G., Németh, Z., Erdős, G., Kis, A., & Dandouras, I. (2009). A global study of hot flow anomalies using cluster multi-spacecraft measurements. *Annales Geophysicae*, 27(5), 2057–2076. <https://doi.org/10.5194/angeo-27-2057-2009>
- Gingell, I., Schwartz, S. J., Burgess, D., Johlander, A., Russell, C. T., Burch, J. L., et al. (2017). MMS observations and hybrid simulations of surface ripples at a marginally quasi-parallel shock. *Journal of Geophysical Research: Space Physics*, 122(11), 11003–11017. <https://doi.org/10.1002/2017JA024538>
- Goncharov, O., Gunell, H., Hamrin, M., & Chong, S. (2020). Evolution of high-speed jets and plasmoids downstream of the quasi-perpendicular bow shock. *Journal of Geophysical Research: Space Physics*, 125(6), e2019JA027667. <https://doi.org/10.1029/2019JA027667>
- Guo, J., Lu, S., Lu, Q., Lin, Y., Wang, X., Ren, J., et al. (2022). Large-scale high-speed jets in earth's magnetosheath: Global hybrid simulations. *Journal of Geophysical Research: Space Physics*, 127(6), e2022JA030477. <https://doi.org/10.1029/2022JA030477>
- Gutynska, O., Sibeck, D. G., & Omid, N. (2015). Magnetosheath plasma structures and their relation to foreshock processes. *Journal of Geophysical Research: Space Physics*, 120(9), 7687–7697. <https://doi.org/10.1002/2014JA020880>
- Hao, Y., Lembege, B., Lu, Q., & Guo, F. (2016). Formation of downstream high-speed jets by a rippled nonstationary quasi-parallel shock: 2-D hybrid simulations. *Journal of Geophysical Research: Space Physics*, 121(3), 2080–2094. <https://doi.org/10.1002/2015JA021419>
- Harvey, C. C. (1998). Spatial gradients and the volumetric tensor. In G. Paschmann & P. W. Daly (Eds.), *Analysis methods for multi-spacecraft data* (p. 307). ESA Publications Division.
- Hietala, H., Laitinen, T. V., Andr  ev  , K., Vainio, R., Vaivads, A., Palmroth, M., et al. (2009). Supermagnetosonic jets behind a collisionless quasiparallel shock. *Physical Review Letters*, 103(24), 245001. <https://doi.org/10.1103/PhysRevLett.103.245001>
- Hietala, H., Phan, T. D., Angelopoulos, V., Oieroset, M., Archer, M. O., Karlsson, T., & Plaschke, F. (2018). In situ observations of a magnetosheath high-speed jet triggering magnetopause reconnection. *Geophysical Research Letters*, 45(4), 1732–1740. <https://doi.org/10.1002/2017GL076525>
- Hietala, H., & Plaschke, F. (2013). On the generation of magnetosheath high-speed jets by bow shock ripples. *Journal of Geophysical Research: Space Physics*, 118(11), 7237–7245. <https://doi.org/10.1002/2013JA019172>
- Horbury, T. S., Burgess, D., Fr  nz, M., & Owen, C. J. (2001). Three spacecraft observations of solar wind discontinuities. *Geophysical Research Letters*, 28(4), 677–680. <https://doi.org/10.1029/2000GL000121>
- Johlander, A., Schwartz, S. J., Vaivads, A., Khotyaintsev, Y. V., Gingell, I., Peng, I. B., et al. (2016). Rippled quasiperpendicular shock observed by the magnetospheric multiscale spacecraft. *Physical Review Letters*, 117(16), 165101. <https://doi.org/10.1103/PhysRevLett.117.165101>
- Kajdi  , P., Raptis, S., Blanco-Cano, X., & Karlsson, T. (2021). Causes of jets in the quasi-perpendicular magnetosheath. *Geophysical Research Letters*, 48(13), e2021GL093173. <https://doi.org/10.1029/2021GL093173>
- K  hnel, W., & Hunt, B. (2015). *Differential geometry: Curves—surfaces—manifolds* (3rd ed.). American Mathematical Society.
- Lin, Y. (2002). Global hybrid simulation of hot flow anomalies near the bow shock and in the magnetosheath. *Planetary and Space Science*, 50(5–6), 577–591. [https://doi.org/10.1016/S0032-0633\(02\)00037-5](https://doi.org/10.1016/S0032-0633(02)00037-5)
- Liu, Y. Y., Fu, H. S., Liu, C. M., Wang, Z., Escoubet, P., Hwang, K.-J., et al. (2019). Parallel electron heating by tangential discontinuity in the turbulent magnetosheath. *The Astrophysical Journal Letters*, 877(2), L16. <https://doi.org/10.3847/2041-8213/ab1fe6>
- McComas, D. J., Bame, S. J., Barker, P., Feldman, W. C., Phillips, J. L., Riley, P., & Griffee, J. W. (1998). Solar wind electron proton alpha monitor (SWEPAM) for the advanced composition explorer. *Space Science Reviews*, 86(1), 563–612. <https://doi.org/10.1023/A:1005040232597>
- Omelchenko, Y. A., Chen, L.-J., & Ng, J. (2021). 3D space-time adaptive hybrid simulations of magnetosheath high-speed jets. *Journal of Geophysical Research: Space Physics*, 126(7), e2020JA029035. <https://doi.org/10.1029/2020JA029035>
- Omid, N., Lee, S. H., Sibeck, D. G., Turner, D. L., Liu, T. Z., & Angelopoulos, V. (2020). Formation and topology of foreshock bubbles. *Journal of Geophysical Research: Space Physics*, 125(9), e2020JA028058. <https://doi.org/10.1029/2020JA028058>
- Omid, N., & Sibeck, D. G. (2007). Formation of hot flow anomalies and solitary shocks. *Journal of Geophysical Research*, 112(A1), A01203. <https://doi.org/10.1029/2006JA011663>
- Parker, E. N. (1958). Dynamics of the interplanetary gas and magnetic fields. *The Astrophysical Journal*, 128, 664. <https://doi.org/10.1086/146579>
- Plaschke, F., Hietala, H., Archer, M., Blanco-Cano, X., Kajdi  , P., Karlsson, T., et al. (2018). Jets downstream of collisionless shocks. *Space Science Reviews*, 214(5), 81. <https://doi.org/10.1007/s11214-018-0516-3>
- Plaschke, F., Hietala, H., & V  r  s, Z. (2020). Scale sizes of magnetosheath jets. *Journal of Geophysical Research: Space Physics*, 125(9), e2020JA027962. <https://doi.org/10.1029/2020JA027962>
- Preisser, L., Blanco-Cano, X., Kajdi  , P., Burgess, D., & Trotta, D. (2020). Magnetosheath jets and plasmoids: Characteristics and formation mechanisms from hybrid simulations. *The Astrophysical Journal Letters*, 900(1), L6. <https://doi.org/10.3847/2041-8213/abad2b>
- Raptis, S., Karlsson, T., Plaschke, F., Kullen, A., & Lindqvist, P.-A. (2020). Classifying magnetosheath jets using MMS: Statistical properties. *Journal of Geophysical Research: Space Physics*, 125(11), e2019JA027754. <https://doi.org/10.1029/2019JA027754>

- Raptis, S., Karlsson, T., Vaivads, A., Pollock, C., Plaschke, F., Johlander, A., et al. (2022). Downstream high-speed plasma jet generation as a direct consequence of shock reformation. *Nature Communications*, 13(1), 598. <https://doi.org/10.1038/s41467-022-28110-4>
- Rème, H., Bosqued, J. M., Sauvaud, J. A., Cros, A., Dandouras, J., Aoustin, C., et al. (1997). The cluster ion spectrometry (CIS) experiment. *Space Science Reviews*, 79(1/2), 303–350. <https://doi.org/10.1023/A:1004929816409>
- Savin, S., Amata, E., Zelenyi, L., Lutsenko, V., Safrankova, J., Nemecek, Z., et al. (2012). Super fast plasma streams as drivers of transient and anomalous magnetospheric dynamics. *Annales Geophysicae*, 30(1), 1–7. <https://doi.org/10.5194/angeo-30-1-2012>
- Schwartz, S. (1995). Hot flow anomalies near the Earth's bow shock. *Advances in Space Research*, 15(8–9), 107–116. [https://doi.org/10.1016/0273-1177\(94\)00092-F](https://doi.org/10.1016/0273-1177(94)00092-F)
- Schwartz, S. J., Paschmann, G., Sckopke, N., Bauer, T. M., Dunlop, M., Fazakerley, A. N., & Thomsen, M. F. (2000). Conditions for the formation of hot flow anomalies at Earth's bow shock. *Journal of Geophysical Research*, 105(A6), 12639–12650. <https://doi.org/10.1029/1999JA000320>
- Shen, C., Zeng, G., Zhang, C., Rong, Z., Dunlop, M., Russell, C. T., et al. (2020). Determination of the configurations of boundaries in space. *Journal of Geophysical Research: Space Physics*, 125(9), e2020JA028163. <https://doi.org/10.1029/2020JA028163>
- Smith, C. W., L'Heureux, J., Ness, N. F., Acuña, M. H., Burlaga, L. F., & Scheifele, J. (1998). The ACE magnetic fields experiment. *Space Science Reviews*, 86(1), 613–632. <https://doi.org/10.1023/A:1005092216668>
- Sonnerup, B. U. O., & Scheible, M. (1998). Minimum and maximum variance analysis. In G. Paschmann & P. W. Daly (Eds.), *Analysis methods for multi-spacecraft data* (p. 185). ESA Publications Division.
- Stone, E. C., Frandsen, A. M., Mewaldt, R. A., Christian, E. R., Margolies, D., Ormes, J. F., & Snow, F. (1998). The advanced composition explorer. *Space Science Reviews*, 86(1), 1–22. <https://doi.org/10.1023/A:1005082526237>
- Thomas, V. A., Winske, D., Thomsen, M. F., & Onsager, T. G. (1991). Hybrid simulation of the formation of a hot flow anomaly. *Journal of Geophysical Research*, 96(A7), 11625–11632. <https://doi.org/10.1029/91JA01092>
- Vuorinen, L., Hietala, H., & Plaschke, F. (2019). Jets in the magnetosheath: IMF control of where they occur. *Annales Geophysicae*, 37(4), 689–697. <https://doi.org/10.5194/angeo-37-689-2019>
- Wang, S., Zong, Q., & Zhang, H. (2013). Cluster observations of hot flow anomalies with large flow deflections: 2. Bow shock geometry at HFA edges. *Journal of Geophysical Research: Space Physics*, 118(1), 418–433. <https://doi.org/10.1029/2012JA018204>
- Zhang, H., Sibeck, D. G., Zong, Q.-G., Gary, S. P., McFadden, J. P., Larson, D., et al. (2010). Time history of events and macroscale interactions during substorms observations of a series of hot flow anomaly events. *Journal of Geophysical Research*, 115(A12), A12235. <https://doi.org/10.1029/2009JA015180>
- Zhao, L. L., Zhang, H., & Zong, Q.-G. (2017). A statistical study on hot flow anomaly current sheets. *Journal of Geophysical Research: Space Physics*, 122(1), 235–248. <https://doi.org/10.1002/2016JA023319>
- Zhao, L. L., Zong, Q. G., Zhang, H., & Wang, S. (2015). Case and statistical studies on the evolution of hot flow anomalies. *Journal of Geophysical Research: Space Physics*, 120(8), 6332–6346. <https://doi.org/10.1002/2014JA020862>